Simplify your imaging workflows

Make research imaging workflows accessible, traceable, and secure with Athena Software for Core Imaging Facilities.

Thermo Scientific™ Athena Software is a premium imaging data management platform designed for core imaging facilities that support materials science research.

Athena Software ensures traceability of images, metadata, and experimental workflows through an intuitive and collaborative web interface.

Find out more at **thermofisher.com/athena**

ThermoFisher SCIENTIFIC

ADVANCED FUNCTIONAL MATERIALS
www.afm-journal.de

Template-Sacrificed Hot Fusion Construction and Nanoseed Modification of 3D Porous Copper Nanoscaffold Host for Stable-Cycling Lithium Metal Anodes

Huinan Lin, Zewen Zhang, Yaoda Wang, Xiao Li Zhang, Zuoxiu Tie, and Zhong Jin**

Lithium (Li) metal anodes have been proposed as a promising candidate for high-energy-density electrode materials in secondary batteries. However, the dendrite growth and unstable electrode–electrolyte interfaces during Li plating/stripping are fatal to their practical applications. Herein, the construction of 3D porous Au/Cu nanoscaffold prepared via a convenient template-sacrificed hot fusion construction method and a nanoseed modification process as an effective Li metal hosting material are proposed. The Au/Cu nanoscaffold can spatially guide uniform deposition of Li metal free from the growth of Li dendrites due to the homogenous Li^+ ion flux and negligible nucleation overpotential. Moreover, the Cu skeleton can relieve volume change and stabilize local current density during cycling processes. Benefiting from these advantages, the symmetric cells based on self-supported Li-filled Au/Cu (Li-Au/Cu) nanoscaffold electrodes present highly stable Li plating/stripping for more than 1000 h with a low voltage hysteresis less than 90 mV and a long lifespan over 1300 h at 1.0 mA cm^{-2} in carbonate-based electrolytes. Impressively, the Li-Au/Cu nanoscaffold||$LiFePO_4$ full cells also exhibit exceptional cycling stability and rate performance. This work provides a promising strategy to construct dendrite-free lithium metal anodes toward high-performance lithium metal batteries.

1. Introduction

The past century has witnessed the great progress in the development of integral energy storage devices with greatly improved performance and environmentally friendliness.[1–6] Rechargeable lithium metal batteries (LMBs) open up new opportunities for the development of high-energy-density electrochemical power sources on both gravimetric and volumetric bases.[7–9] Unfortunately, the uneven Li electrodeposition and inevitable side reactions within organic electrolyte reduce the capacity and Coulombic efficiency (CE) during long-time charging/discharging cycling.[10,11] Moreover, the severe dendritic Li growth can even penetrate the separator to cause a short circuit in the cell, resulting in a catastrophic and dangerous failure.[12,13] To overcome the bottleneck of LMBs, the achieving of a stable and efficient lithium metal anode is urgently needed. Recently, plenty of potential strategies have been developed to alleviate the growth of Li dendrite, including optimizing electrolyte compositions,[14–16] constructing protective artificial solid-electrolyte interfaces (SEI),[17–19] designing 3D Li-host materials,[20–22] employing solid-state electrolytes,[23–25] and functional separator modifications.[26,27] Among these approaches, a research hotspot for guiding homogeneous Li electrodeposition is the introduction of 3D porous and conductive scaffolds, which can not only accommodate volume change during Li plating/stripping, but also enable stable cycling performance originated from homogeneous current density.[13,28–31] Besides, it has been reported that some Li-host substrates with low Li nucleation overpotential, such as, Au and silver nanostructures,[32,33] CuO nanowire arrays,[34] and nitrogen-doped graphene[35] can modulate the surface energy and eliminate nucleation barriers to inhibit Li dendrite formation. According to the aforementioned discussion, it can be deduced that an ideal 3D scaffold for Li deposition should possess the following merits: 1) High surface area and large free space for reducing the local current density and buffering the volumetric expansion during Li plating/stripping processes; 2) abundant Li nucleation sites with low overpotential for Li deposition to render the dendrite-free morphology; 3) high conductivity and integrative conductive network for improving charge transfer and reducing the interfacial resistance; 4) strong mechanical and electrochemical stability during long-term cycling processes; 5) low cost and simple fabrication process for commercialization.

Herein, we report a convenient strategy for the fabrication of gold nanoseed decorated 3D porous copper (Au/Cu) nanoscaffold via a template-sacrificed hot fusion construction method

H. Lin, Z. Zhang, Y. Wang, Dr. Z. Tie, Prof. Z. Jin
MOE Key Laboratory of Mesoscopic Chemistry
MOE Key Laboratory of High Performance Polymer Materials and Technology
Jiangsu Key Laboratory of Advanced Organic Materials
School of Chemistry and Chemical Engineering
Nanjing University
Nanjing 210023, China
E-mail: zxtie@nju.edu.cn; zhongjin@nju.edu.cn

H. Lin, Z. Zhang, Y. Wang, Dr. Z. Tie, Prof. Z. Jin
Shenzhen Research Institute of Nanjing University
Shenzhen 518057, China

Prof. X. L. Zhang
School of Materials Science and Engineering
Zhengzhou University
Zhengzhou 450001, China

The ORCID identification number(s) for the author(s) of this article can be found under https://doi.org/10.1002/adfm.202102735.

DOI: 10.1002/adfm.202102735

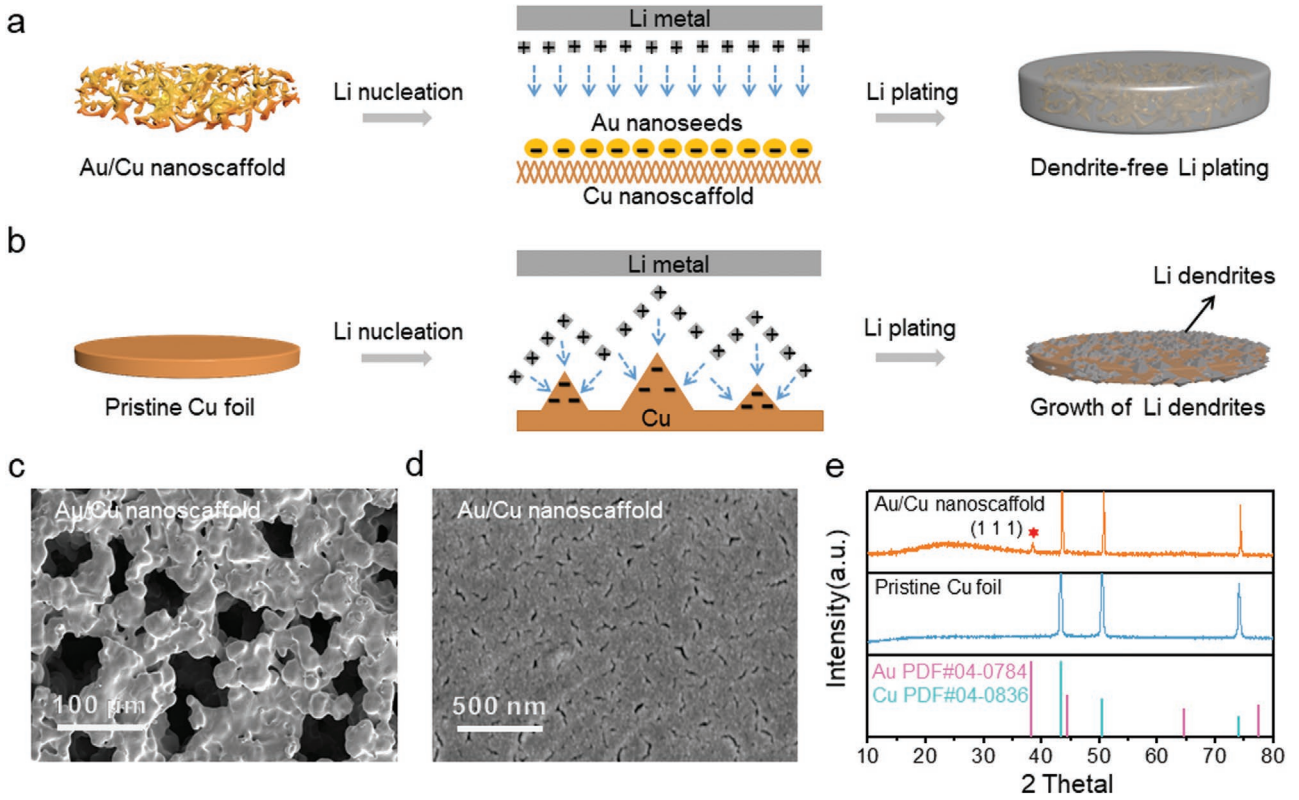

Figure 1. Schematic illustration of Li nucleation and plating processes on a) Au/Cu nanoscaffold and b) pristine Cu foil. c,d) SEM images of Au/Cu nanoscaffold. e) XRD patterns of Au/Cu nanoscaffold and pristine Cu nanoscaffold.

and a thermal evaporation approach. The Au/Cu nanoscaffold can serve as a promising self-supported current collector for suppressing Li dendrite formation (**Figure 1**a). The porous structure of 3D-interconnected Cu skeleton (Figure S1a,c, Supporting Information) can provide a large void space for metallic Li storage and effectively alleviate the large volume changes during Li plating/stripping processes. Meanwhile, the Cu skeleton with high porosity exhibits an attractive characteristic of reducing the local current density, which contributes to more uniform charge distribution, and thus smoothens Li electrodeposition.[29,30,36] Furthermore, the Au nanoseeds decorating on Cu skeleton play a key role as uniformly dispersed nucleation sites, capable of further guiding the homogeneous deposition of Li^+ ions. Meanwhile, the characterization results in this work confirm that the Au nanoseeds react with deposited Li to form Li_xAu_y alloy phase, which is able to modulate the surface energy and eliminate nucleation barriers to further inhibit dendritic Li formation. Benefited from these merits, the Li metal infused Au/Cu nanoscaffold anode exhibits impressive rate performance and remarkably improved cycle stability in conventional carbonate-based electrolyte.

2. Results and Discussion

The 3D porous Au/Cu nanoscaffold was prepared by an elaborately-designed template-sacrificed hot fusion construction method and following by thermal decoration of Au nanoseeds, as detailed in the Experimental Section. First, atomized Cu powder was mixed with polyurethane powder (used as sacrificial template) and heated at 600 °C in O_2 atmosphere. During this step, the atomized Cu powder was fused together to form 3D interconnected Cu skeleton, and then polyurethane powder was oxidized and decomposed to gases. Second, a subsequent H_2 treatment at 1000 °C was performed to remove the surface oxidation layer of Cu skeleton, forming the pristine Cu nanoscaffold. Third, Au nanoseeds were decorated on the Cu skeleton via thermal evaporation to form the Au/Cu nanoscaffold. Compared with the pristine Cu foil normally used as current collector in the conventional design of Li metal batteries, the elaborately prepared Cu nanoscaffold as a 3D interconnected framework (Figure 1a and Figure S1a,c, Supporting Information) can serve as a superior current collector for facilitating charge transfer and furnishing a large porosity and free space. This is because that the uneven surface of pristine Cu foils (Figure 1b and Figure S1b,d, Supporting Information) will inevitably lead to inhomogeneous charge flux, and the random nucleation sites of Cu foil will bring about uneven ionic flux, which directly account for nonuniform Li deposition and finally severe dendritic Li growth. In contrast, the 3D-interconnected pores of Cu nanoscaffold are favor of suppressing Li dendrite growth and alleviating the volume changes of Li plating/stripping. The fabricated 3D porous Cu nanoscaffold retains the granular morphology of atomized Cu powder, which is conducive to increasing the electrochemically active surface area of the Cu nanoscaffold, so that the electric charge distribution

is more uniform and the deposited Li can better wet the Cu nanoscaffold. Moreover, the components, porosity, skeleton structure, and thickness of the metallic nanoscaffold can be easily and extensively adjusted by changing the preparation conditions of template-sacrificed hot fusion construction method, bringing a much wider range of freedom for the structure and performance regulation than commercial Cu foam. Nevertheless, since metallic Cu is lithiophobic, the relatively low lithium wettability and high nucleation barrier of pristine Cu skeleton are not conducive to Li deposition during long-term cycling. To tackle the problems faced by pristine Cu skeleton, facile decoration of Au nanoseeds was further applied on Cu nanoscaffold to increase its lithiophilicity and Li-nucleation sites (Figure 1a). Scanning electron microscope (SEM) and energy dispersive X-ray spectrometer characterizations (Figure 1c,d and Figure S1e–g, Supporting Information) intuitively verified the uniform dispersion of Au nanoseeds on 3D porous Cu skeleton, providing preferential nucleation sites for Li deposition. X-ray diffraction (XRD) was also used to character the Au/Cu nanoscaffold (Figure 1e). The diffraction peaks at 43.3°, 50.4°, and 74.1° could be ascribed to Cu metal (PDF#04-0836) of (111), (200), and (220) planes.[34] The XRD peaks at 43.3° is in accord with the (111) planes of Au metal (PDF#04-0784), confirming the deposition of Au nanoseeds on the Cu skeleton.[37,38]

As shown in **Figure 2**, the electrochemical performances of Li||Cu half cells using three different current collectors were systematically investigated. First of all, the CE of the cells was tested to demonstrate the enhanced Li utilization during Li plating/stripping in case of using Au/Cu nanoscaffold (Figure 2a). The cells were first cycled between 0 and 1.0 V

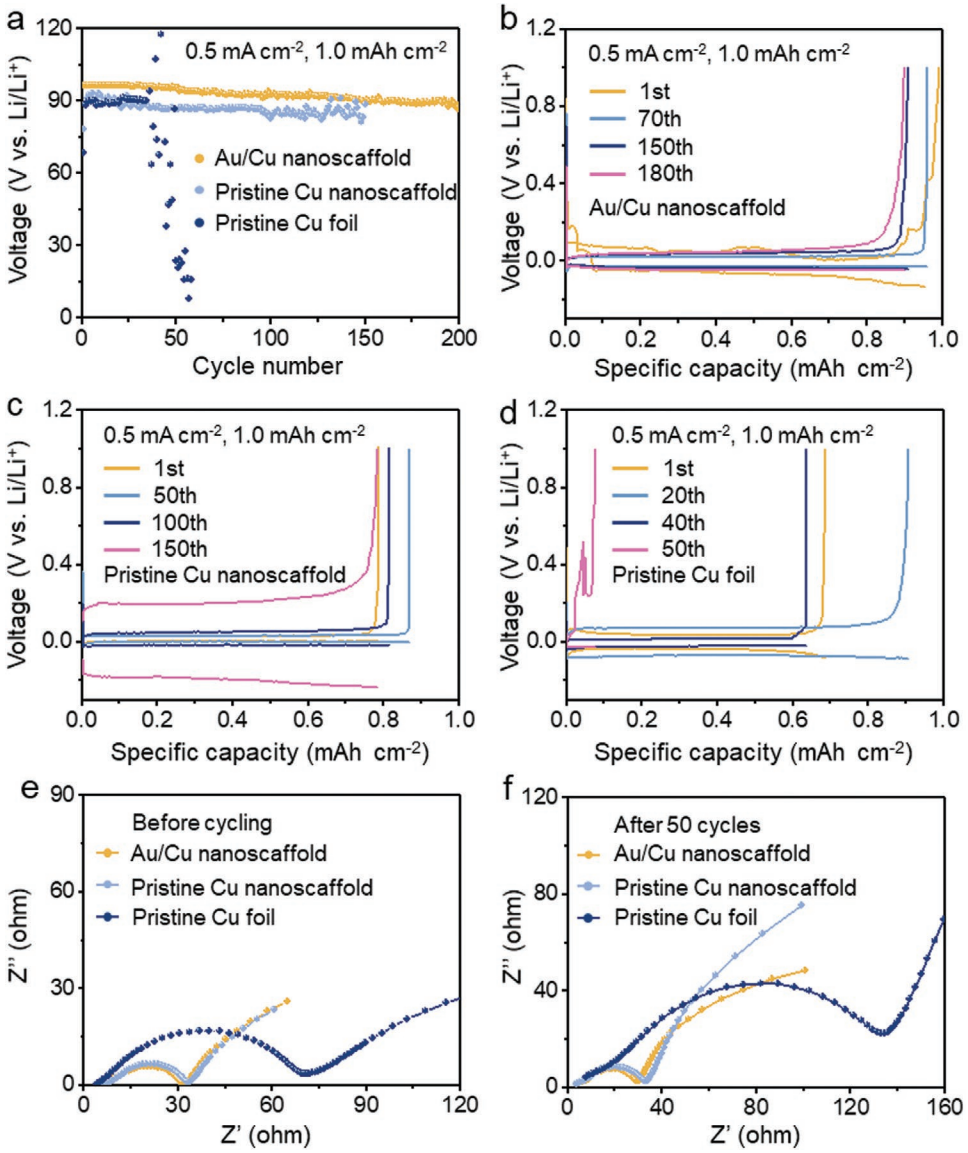

Figure 2. a) CE of Li||Cu half cells assembled with Au/Cu nanoscaffold, pristine Cu nanoscaffold, and pristine Cu foil current collectors measured at a current density of 0.5 mA cm^{-2} with a capacity of 1.0 mAh cm^{-2}. Voltage profiles of Li plating/stripping processes on b) Au/Cu nanoscaffold, c) pristine Cu nanoscaffold, and d) pristine Cu foil current collectors during different cycles. EIS spectra of Li||Cu half cells assembled with Au/Cu nanoscaffold, pristine Cu nanoscaffold, and pristine Cu foil current collectors e) before and f) after 50 cycles.

(vs Li^+/Li) at the current density of 0.05 mA cm^{-2} for 2 cycles to form a layer of stable SEI. Figure S2, Supporting Information, shows the CE of the cells using Au/Cu nanoscaffold decorated with different sizes of Au nanoseeds (10–70 nm in diameter). Meanwhile, SEM images also displayed the distinct morphologies of long-term cycled Au/Cu nanoscaffold decorated with different sizes of Au nanoseeds and corresponding Li foil counter electrodes (Figure S3, Supporting Information). Obviously, the Au/Cu nanoscaffold modified with Au nanoseeds of 50 nm diameter exhibited the best Li utilization efficiency and Li deposition uniformity during the cycling processes. Therefore, the Au/Cu nanoscaffold coated with 50-nm-diamenter Au nanoseeds was adopted for the following tests. The CE of the Li‖Cu half cells with Au/Cu nanoscaffold, pristine Cu nanoscaffold and pristine Cu foil current collectors were tested at 0.5 mA cm^{-2} with a capacity of 1.0 mAh cm^{-2}, as displayed in Figure 2a. The cells based on pristine Cu foil current collectors presented the worst Li utilization efficiency, and a marked reduction of the CE was observed after 40 cycles. In contrary, the cells assembled with pristine Cu nanoscaffold showed greatly improved CE and prolonged lifetime. Furthermore, the cells with Au/Cu nanoscaffold exhibited the best cycling stability and longest lifetime with the CE of 87% after 200 cycles. The voltage profiles of Li plating/stripping on pristine Cu foil, pristine Cu nanoscaffold, and Au/Cu nanoscaffold were displayed in the Figure 2b–d. Compared with the pristine Cu foil and Cu nanoscaffold, the Au/Cu nanoscaffold showed excellent Li plating/stripping behaviors with a small overpotential of 78 mV after 180 cycles (Figure 2b), suggesting Au nanoseeds played a key role in the improvement of cycling stability and electrochemical kinetic performance. To further verify the outstanding performance of Au/Cu nanoscaffold as current collector, the CEs at higher current densities (1.0 and 2.0 mA cm^{-2}) or with larger areal specific capacity (2.0 mAh cm^{-2}) were also measured (Figure S4a–c, Supporting Information). Expectedly, the half cells using Au/Cu nanoscaffold current collector not only possessed the highest CE but also presented the greatly improved cycling life and stability. Compared to the CEs of other asymmetric cells based on different functional current collectors in previous reports (Table S1, Supporting Information), the electrochemical performances of Au nanoseeds modified 3D porous Cu nanoscaffold is very competitive among these results.

To demonstrate the improved electrochemical kinetic behaviors of Au/Cu nanoscaffold, the Nyquist plots of cells assembled with these different current collectors before and after 50 cycles of repeated Li plating/stripping were measured by electrochemical impedance spectroscopy (EIS) (Figure 2e,f). For pristine Cu foil, the charge transfer resistance of the cells increased sharply from 67.0 to 126.4 Ω after 50 cycles. When using pristine Cu nanoscaffold as the current collector, the charge transfer resistances before and after 50 cycles were 27.5 and 29.6 Ω, respectively, confirming that the Cu skeleton is able to facilitate the charge transfer process due to its 3D interconnected structure. Notably, the charge transfer resistance of the cells assembled with Au/Cu nanoscaffold was 25.1 Ω, which only slightly increased to 25.6 Ω. Moreover, it is revealed that the uniformly dispersed Au nanoseeds can provide abundant nucleation sites for the deposition of Li metal, which not only speeds up the reaction kinetics, but also renders the Li deposition more uniform. Therefore, the Au/Cu nanoscaffold current collector is conducive to the achieving of improved Li plating/stripping behaviors and the inhibition of dendritic Li nucleation and growth.

Superior Li wettability of a current collector is perceived as an important guarantee excellent electrochemical kinetics. As shown in **Figure 3**a, the introduction of Au nanoseeds significantly improved the Li wettability of Au/Cu nanoscaffold, which intuitively proved the superiority of Au/Cu nanoscaffold as the current collector of Li metal anodes. In addition, the initial Li deposition overpotential was investigated in detail to reveal the Li deposition behaviors with different current collectors. Generally, the initial Li deposition overpotential includes the mass-transfer overpotential and the nucleation overpotential.[35,36] The mass-transfer overpotential originated from mass-transfer resistance is related to the current density and the mobility of Li^+ ions, while the nucleation overpotential reflects the level of energy barrier to be overcome during the Li nucleation process. According to the voltage-capacity curves shown in Figure 3b, at the initial stage of Li deposition on pristine Cu foil at 0.05 mA cm^{-2}, a sharp drop in voltage to –0.190 V related to the nucleation of Li metal was observed. After the nucleation process, the voltage platform slowly rose to a fairly steady value of –0.152 V, representing the mass-transfer overpotential. The difference between –0.190 and –0.152 V was ≈38 mV, which is considered as the nucleation overpotential on pristine Cu foil. For pristine Cu nanoscaffold, the nucleation overpotential at the initial stage of Li deposition was 48 mV. It was worth noting that a zero nucleation overpotential was obtained in case of using Au/Cu nanoscaffold, which implied that the deposited Li metal was likely to react with Au nanoseeds to form Li_xAu_y alloy phase during the Li deposition. Although the mass-transfer overpotential rose with the increase of current densities, the zero nucleation overpotential was well maintained at higher current densities when using Au/Cu nanoscaffold as the current collector (Figure 3c). The initial Li deposition overpotentials of these different current collectors at different current densities were compared in detail (Figure 3d). Consequently, the Au/Cu nanoscaffold exhibited the minimum Li deposition overpotential at all the current densities, indicating that the synergetic effect of Cu skeleton and Au nanoseeds prominently reduced the energy barrier of Li nucleation and improved the mass-transfer kinetics of the current collector.

To verify the alloying of Li metal with Au nanoseeds during the initial stage of Li deposition, cyclic voltammetry (CV) curves of Li‖Cu half cells based on Au/Cu nanoscaffold and pristine Cu nanoscaffold were measured (Figure S5, Supporting Information). The CV scanning range from 0 to 1.0 V was selected to avoid the Li metal deposition and SEI oxidative decomposition. As a result, the CV curve of the cells with Au/Cu nanoscaffold showed three marked cathodic peaks and two marked anodic peaks compared with those with pristine Cu nanoscaffold. It has been reported that the cathodic process at the potentials of 0.2 to 0 V corresponds to the insertion of lithium into gold to form Li_xAu_y alloys (such as, Au_5Li_4, AuLi, $AuLi_2$, $AuLi_3$, and Au_4Li_{15}), whereas the anodic process in the potential range from 0 to 0.7 V corresponds to the lithium extraction.[39] Therefore, the peaks in the CV curve in case of using Au/Cu

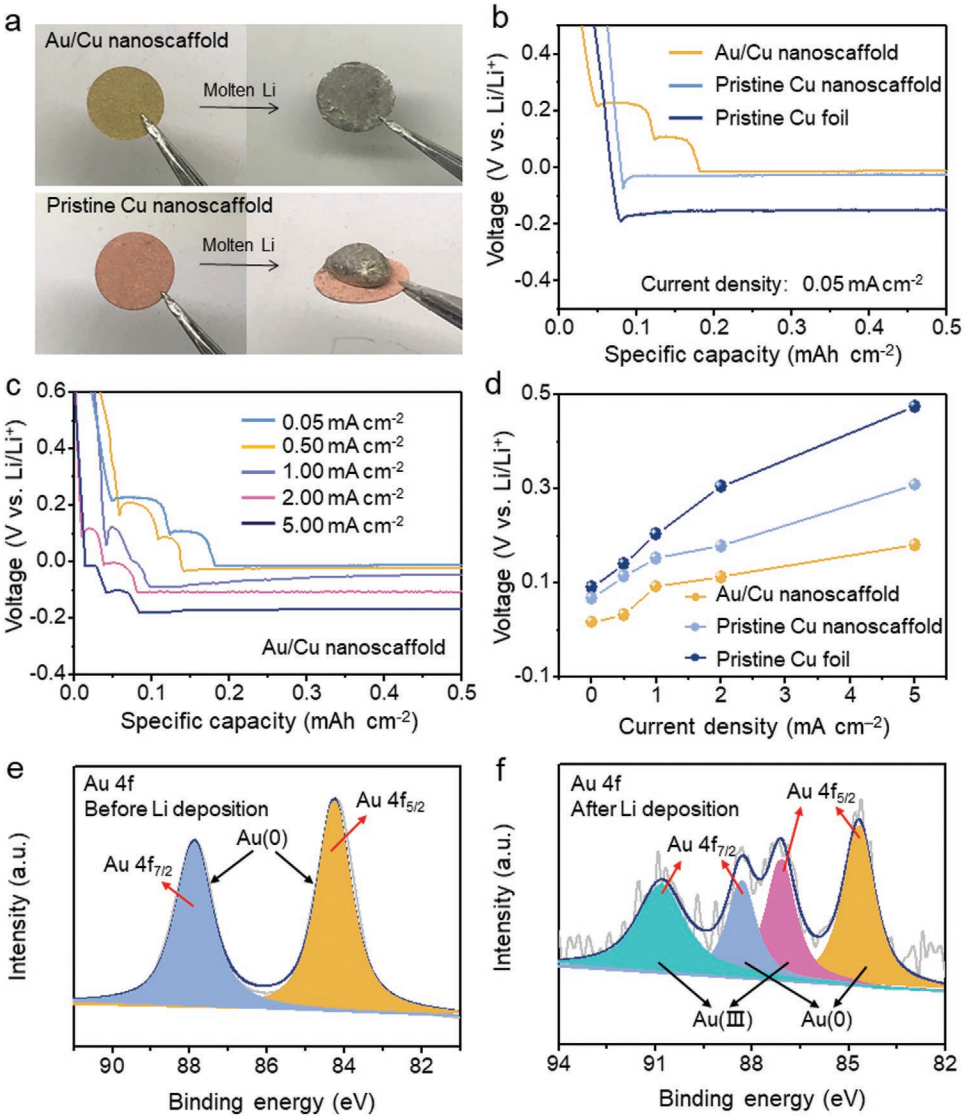

Figure 3. a) Visual comparison of Li wettability of Au/Cu nanoscaffold and pristine Cu nanoscaffold. b) Initial Li plating profiles of Li||Cu cells assembled with Au/Cu nanoscaffold, pristine Cu nanoscaffold and pristine Cu foil at a current density of 0.05 mA cm^{-2}. c) Initial Li plating profiles of Li||Cu cells assembled with Au/Cu nanoscaffold at different current densities. d) Comparison of initial Li deposition overpotential of Au/Cu nanoscaffold, pristine Cu nanoscaffold, and pristine Cu foil at different current densities. High-resolution Au 4f XPS spectra of Au/Cu nanoscaffold e) before Li deposition and f) after Li deposition.

nanoscaffold corresponded to the formation or disintegration of these intermetallic compounds. The above results conclusively demonstrated that metallic Li could be alloyed with Au nanoseeds to form Li_xAu_y alloys, directly leading to the superior Li deposition behaviors with the zero nucleation overpotential. Moreover, high-resolution X-ray photoelectron spectroscopy was also employed to further verify the alloying of Li metal with Au nanoseeds. Compared with the Au 4f spectrum of the Au/Cu nanoscaffold before Li deposition (Figure 3e), two additional peaks were emerged at 87.1 and 90.7 eV after Li deposition (Figure 3f), corresponding to the Au $4f_{5/2}$ and Au $4f_{7/2}$ bands of Au (III) species.[38] Therefore, it could be concluded that the alloying reactions of Li metal with Au nanoseeds indeed occurred in the initial stage of Li deposition, resulting in a significant enhancement in Li wettability of the Au/Cu nanoscaffold and the improvement of the electrochemical kinetic performance of the electrodes.

To intuitively compare the difference of Li plating behaviors on the Au/Cu nanoscaffold and pristine Cu nanoscaffold, we prepared a special current collector of Cu nanoscaffold with half of its area modified by Au nanoseeds (**Figure 4**). The coin cells assembled with the special current collector as the working electrode and bare Li foil as the counter electrode were galvanostatically discharged at 0.5 mA cm^{-2}. From the photographs and SEM images, it could be seen that the Au nanoseed modified area of the special current collector displayed more uniform and smoother surface with the Li plating capacities of 2.0 mAh cm^{-2} (Figure 4a,m). As the Li deposition capacity increased to 5.0 mAh cm^{-2} (Figure 4b,n), the Au nanoseed modified area well preserved smooth and flat deposition

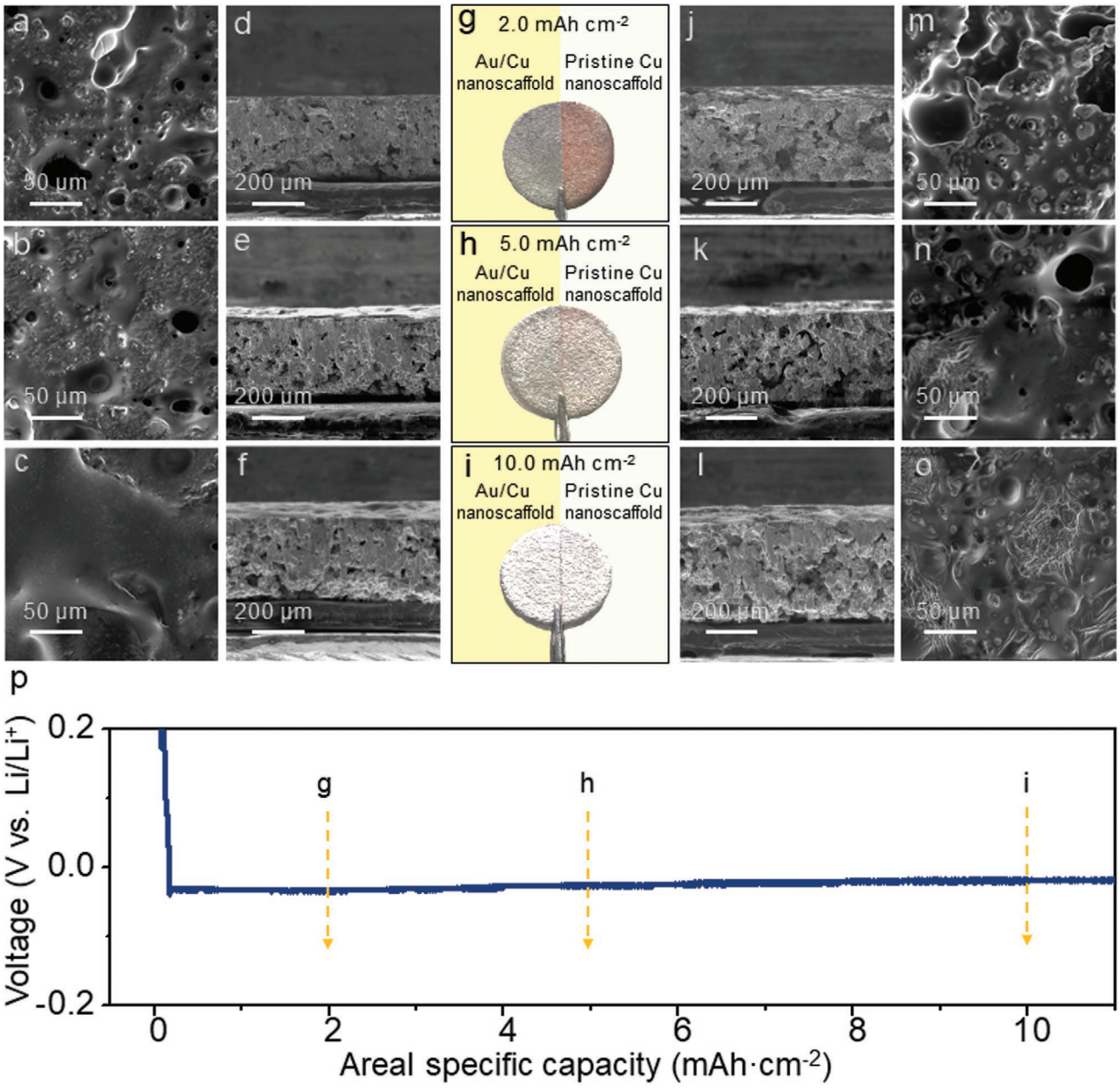

Figure 4. Morphology evolution of a special current collector (Cu nanoscaffold with half of its area decorated with Au nanoseeds) at the different stages of Li plating. a–c) Top-section and d–f) cross-section SEM images of the Au nanoseed modified area with different Li plating capacities of a,d) 2.0, b,e) 5.0, and c,f) 10.0 mAh cm^{-2}. g–i) Photographs of the special current collector with different Li plating capacities of 2.0, 5.0, and 10.0 mAh cm^{-2}, respectively. j–l) Top-section and m–o) cross-section SEM images of the bare area (without Au nanoseed modification) with different Li plating capacities of j,m) 2.0, k,n) 5.0, and l,o) 10.0 mAh cm^{-2}. p) voltage-capacity profile of the Li deposition process on the special current collector.

morphology, and the void pores without deposited Li were obviously reduced if compared with the bare area. When the Li plating capacities was further increased to 10.0 mAh cm^{-2} (Figure 4c,o), the Au nanoseed modified area presented a dense and dendrite-free morphology, indicating that the modification of Au nanoseeds was helpful to improve the uniformness of Li deposition. Meanwhile, from the cross-section views (Figure 4d–f), the thickness of the nanoseed modified area had almost no change at different Li plating capacities, proving that Li metal had sufficiently infiltrated into the void pores of Au/Cu nanoscaffold rather than deposited on the surface; in contrary, the bare area showed a gradually raising thickness along with the increase of Li plating capacities, indicating the partial Li deposition on the surface (Figure 4g–l). These results further proved the good Li wetting effect of the Au/Cu nanoscaffold than pristine Cu nanoscaffold. The results strongly confirmed that Li metal was preferentially nucleated on Au nanoseeds due to the zero nucleation overpotential, and then gradually filled into the voids of Au/Cu nanoscaffold, forming a smooth Li-filled composite structure without dendrites.

The structural and morphology evolution of Au/Cu nanoscaffold, pristine Cu nanoscaffold and pristine Cu foil after various Li plating/stripping cycles were also characterized by SEM (Figure S6, Supporting Information). After 30 cycles, sharp Li dendrites could be observed on the Cu foil with numerous cracks and protrusions (Figure S6c, Supporting Information). The uneven and unsmooth Li deposition on Cu foil was further aggravated after 100 cycles (Figure S6f, Supporting Information), finally causing the formation of plenty of dead Li.[34,35] The loosely aggregated structure of dead Li not only seriously jeopardized cycling performance but also further accelerated unsmooth and uneven Li deposition. Under the same conditions, a marked improvement of Li deposition morphology was observed when using pristine Cu nanoscaffold as current collector (Figure S6b,e, Supporting Information). A small number of protrusions could still be seen, but overall, the whole surface presented a dense morphology. Especially after 100 cycles (Figure S6e, Supporting Information), it could be found that Li dendrites were significantly inhibited. The improved Li deposition morphology was mainly due to the uniformly distributed porous structure in the pristine Cu nanoscaffold, which not only relieved the volume changes but also induced a homogeneous Li^+ ion flux.[23,24,36] Benefiting from the 3D porous structure of Cu skeleton and excellent Li wettability of Au nanoseeds, a smooth and dense surface without visible microcracks and Li dendrites was observed from Au/Cu nanoscaffold even after 100 cycles of Li plating/stripping (Figure S6d, Supporting Information). Therefore, it can be convincingly concluded that Au/Cu nanoscaffold as the current collector of Li metal anodes has dominant superiority in achieving the uniform Li deposition without dendritic Li, thus resulting in the enhanced cycling stability and lifetime of Li metal anodes.

Encouraged by the intriguing electrochemical performances of Au/Cu nanoscaffold, the cycling stability and rate performance of symmetric batteries using Li-filled Au/Cu (Li-Au/Cu) nanoscaffold, Li-Cu nanoscaffold and bare Li electrodes were further examined (**Figure 5**). All the symmetric cells were first cycled at a constant current density of 0.05 mA cm^{-2} with a total capacity of 1.0 mAh cm^{-2} for 5 cycles to form the stable SEI on the surface of electrodes. As shown in Figure 5a, undesired voltage hysteresis was found in the symmetric batteries assembled with bare Li electrodes after cycling for only 400 h at 1.0 mA cm^{-2} with a capacity of 1.0 mAh cm^{-2}. With the increase of current densities and areal specific capacity, the symmetric batteries based on bare Li electrodes showed obviously deteriorated cycling stability and decreased cycle life (Figure 5b, Figure S7a–c, Supporting Information). When using Li-Cu nanoscaffold as the electrodes, the symmetric batteries exhibited prolonged cycling life and improved Li plating/stripping behaviors in contrast to the batteries with bare Li electrodes, but a sharply increased voltage polarization still appeared after cycling for 950 h at 1.0 mA cm^{-2} with a capacity of 1.0 mAh cm^{-2} (Figure 5a). Similarly, the increase of current densities and areal specific capacity also worsened the cycling stability of the batteries with Li-Cu nanoscaffold electrodes (Figure 5b, Figure S7a–c, Supporting Information). In sharp contrast, the symmetric batteries with Li-Au/Cu nanoscaffold electrodes showed stable Li plating/stripping behavior with low voltage hysteresis for over 1300 h at 1.0 mA cm^{-2} with a capacity of 1.0 mAh cm^{-2} (Figure 5a). When the current density increased to 2.0, 3.0, and 5.0 mA cm^{-2}, the batteries still maintained stable voltage profiles for over 660, 270, and 80 h (Figure 5b, Figure S7a,b, Supporting Information). As the areal specific capacity was enhanced to 2.0 mAh cm^{-2}, a stable Li plating/stripping behavior maintained for over 350 h was also obtained (Figure S7c, Supporting Information), indicating the Li-Au/Cu nanoscaffold electrode was greatly conducive to enhancing kinetics performance and guiding the uniform deposition of Li^+ ions, thus improving the stability of continuous Li plating/stripping. Moreover, distinct differences in voltage polarization was further emphasized by the magnified voltage profiles of the symmetric batteries with three different electrodes (Figure S8a–c, Supporting Information). At the current density of 1.0 mA cm^{-2}, the Li-Au/Cu nanoscaffold electrode delivered an overpotential of ≈21.0 mV after cycling for 150 h, which slightly increased to ≈53.0 mV after cycling for 390 h and then to ≈75.0 mV after cycling for 1000 h. However, the bare Li electrode displayed a much higher overpotential after cycling for 150 h, and rapidly resulted in a short circuit after cycling for 390 h. Furthermore, to evaluate the effect of porosity of Au/Cu nanoscaffold on the electrochemical performance of batteries, we have prepared Au/Cu nanoscaffold with different porosity by controlling the weight ratio of atomized Cu powder and polyurethane powder. In the control experiments (Figure S9, Supporting Information), the precursor weight ratio of polyurethane powder and atomized Cu powder to obtain the optimized porosity was determined to be 1:3.4. The testing results showed that the cyclic stability of symmetric cells would be deteriorated if the porosity of Au/Cu nanoscaffold was too high or too low (with a precursor weight ratio of 1:2.8 or 1:4.0). The too high porosity may lead to inhomogeneous Li deposition in the large void space inside Au/Cu nanoscaffold. While the two low porosity will not be able to accommodate enough Li metal, and the complete wetting of Li metal to Au/Cu nanoscaffold becomes more difficult.

The rate performances of the symmetric cells with these Li-filled or bare Li electrodes were also compared at various current densities from 0.5 to 10.0 mA cm^{-2} with a constant capacity of 1.0 mAh cm^{-2} (Figure 5c). With the increase of current density, the bare Li electrodes showed sharply increased voltage polarization, and irregular voltage curves could be observed at the current density of 10 mA cm^{-2}, indicating the symmetric batteries with bare Li electrodes were unable to work stably under such a high current density. Moreover, the short circuit of the symmetric batteries with bared Li electrodes occurred after cycling for 125 h, further confirming that the poor kinetic performance and uneven Li deposition significantly reduced the long-term cycling performance. For Li-Cu nanoscaffold electrodes, a lower voltage hysteresis of ≈600 mV was observed at the high current density of 10.0 mA cm^{-2}. In contrast, the Li-Au/Cu nanoscaffold electrodes showed the lowest and most stable voltage polarizations of 20, 70, 100, 150, and 270 mV at the current densities of 0.5, 1.0, 2.0, 5.0, and 10 mA cm^{-2}, respectively.

The feasibility of Li-Au/Cu nanoscaffold anodes in workable metal Li batteries was verified in Li||$LiFePO_4$ (LFP) full batteries. In the **Figure 6**a, the batteries assembled with Li-Au/Cu nanoscaffold anodes exhibited stable cycling behaviors with the highest discharge specific capacity compared with Li-Cu

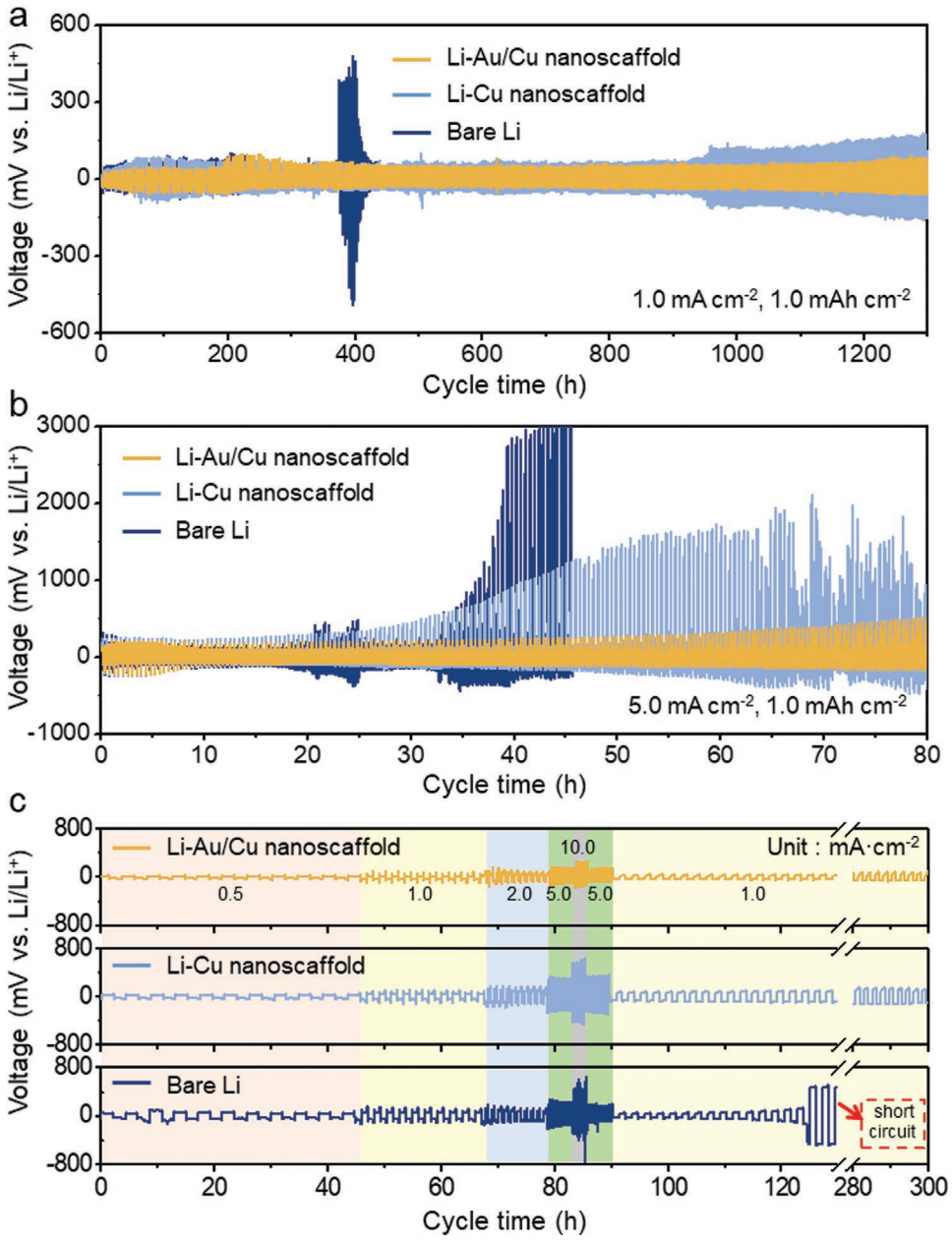

Figure 5. Comparison of the galvanostatic cycling stability of the symmetric batteries assembled with Li-filled Li-Au/Cu nanoscaffold, Li-Cu nanoscaffold, and bare Li electrodes at a) 1.0 mA cm^{-2} and b) 5.0 mA cm^{-2} with a capacity of 1.0 mAh cm^{-2}. c) Rate performance of the symmetric cells with three different electrodes at different current densities of 0.5, 1.0, 2.0, 3.0, and 5.0 mA cm^{-2} with a fixed capacity of 1.0 mAh cm^{-2}.

nanoscaffold and bare Li anodes. The initial discharge capacity of battery with Li-Au/Cu nanoscaffold was 129 mAh g^{-1} at 1.0 C, which was much higher than the batteries using Li-Cu nanoscaffold (114 mAh g^{-1}) or bare Li anodes (111 mAh g^{-1}). Moreover, the batteries with Li-Au/Cu nanoscaffold anodes delivered a high discharge capacity of 126 mAh g^{-1} and obtained a capacity retention of 97.7% after 200 cycles at 1.0 C, whereas the batteries with Li-Cu nanoscaffold anodes presented inferior cycling stability with a lower capacity retention of 77.2%. As for the batteries with the bare Li anodes, more obvious discharge capacity deterioration was experienced, obtaining only a capacity retention of 61.3% after 200 cycles. Significant differences were also observed in term of the CE of the batteries (Figure 6b). A stable CE of more than 98.8% can be obtained for the batteries with Li-Au/Cu nanoscaffold anodes, while the battery using Li-Cu nanoscaffold anodes exhibited an average CE of only 79.6%. When using the bare Li anodes, the CE of the batteries fluctuated obviously during the cycle, and especially after 120 cycles, the CE was significantly reduced to less than 40%. The superior cycling performance and higher average CE of full batteries with Li-Au/Cu nanoscaffold anodes profited from well-designed Li hosting structure with 3D porous Cu skeleton and uniformly dispersed Au nanoseeds. In addition, the Li-Au/Cu nanoscaffold||LPF full batteries also exhibited

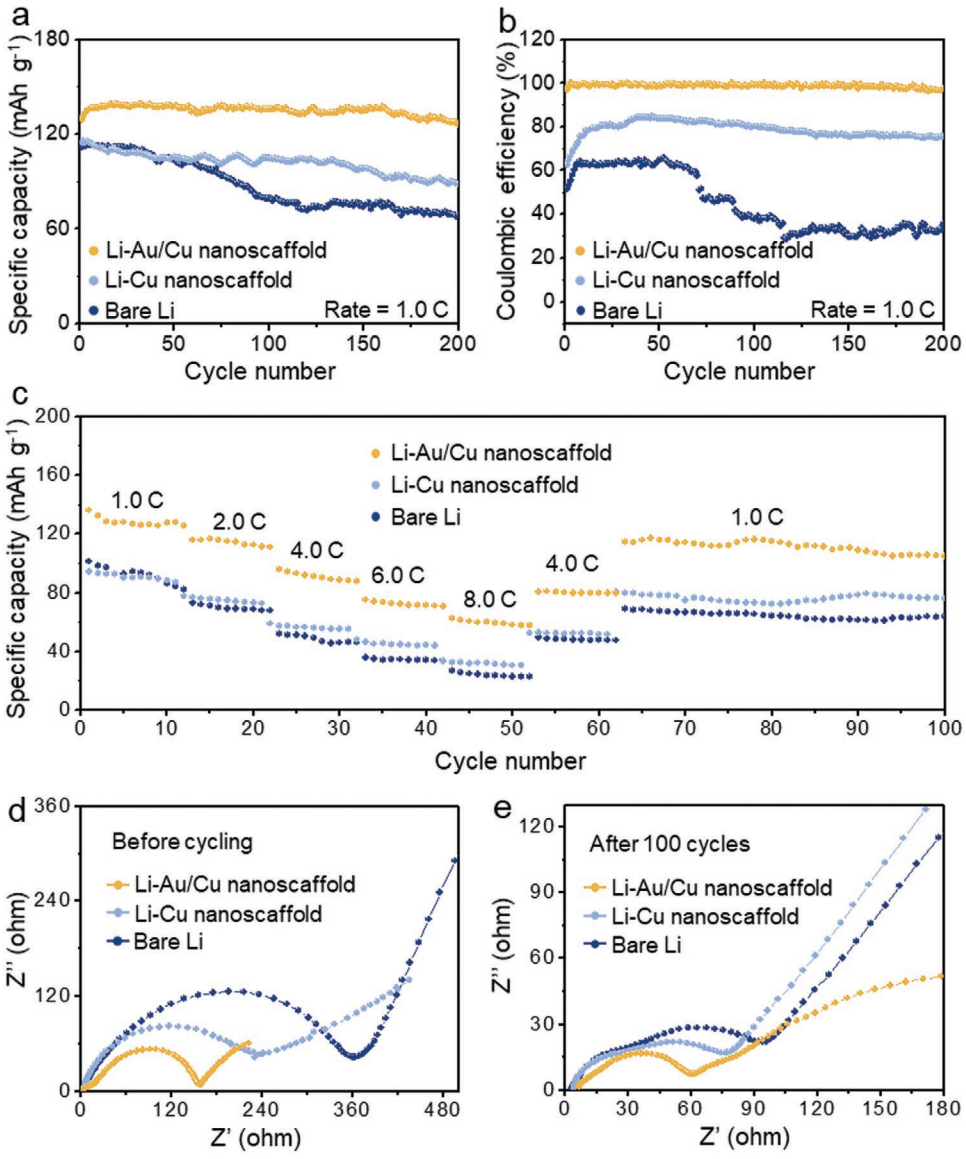

Figure 6. Electrochemical performances of Li||LFP full cells assembled with Li-Au/Cu nanoscaffold, Li-Cu nanoscaffold, or bare Li anodes. a) Discharge specific capacity and b) CE of the Li||LFP full cells at 1.0 C (1.0 C = 170 mA g^{-1}). c) Rate performance of the Li||LFP full cells at various current densities from 1.0 to 8.0 C. EIS spectra of the Li||LFP full cells d) before and e) after 100 cycles.

impressive rate performance (Figure 6c). Specifically, the full batteries with Li-Au/Cu nanoscaffold anodes delivered reversible discharge capacities of 128, 117, 96, 76, and 62 mAh g^{-1} at the increasing current densities of 1.0, 2.0, 4.0, 6.0, and 8.0 C, respectively, and when the current densities returned to 4.0 and 1.0 C, the discharge capacities were well recovered. By comparison, Both the Li-Cu nanoscaffold and the bare Li displayed notably decayed rate performance. Furthermore, the EIS spectra of Li||LFP full cells assembled with three different anodes were also concerned (Figure 6d,e). Before and after 100 cycles, the full batteries with Li-Au/Cu nanoscaffold anodes displayed the minimum interfacial resistance of 157.8 and 60.3 Ω, respectively. For the Li-Au/Cu nanoscaffold||LFP full batteries, it could be concluded that the enhanced mass-transfer kinetics was an important guarantee for the improvement of the discharge capacity and the CE. The electrochemical test results of Li-Au/Cu nanoscaffold||LFP full batteries fully demonstrated the dominant advantages of the Li-Au/Cu nanoscaffold as an advanced Li anode for accelerating kinetic process and prolonging cycle life.

3. Conclusions

In summary, we designed and fabricated an Au nanoseed decorated 3D porous Cu nanoscaffold via a convenient template-sacrificed hot fusion construction method to serve as a high-performance current collector for Li metal anodes. For one thing, the 3D interconnected Cu skeleton in the Au/Cu nanoscaffold can contribute to the uniform charge distribution

and guiding homogeneous deposition of Li^+ ions. For another, uniformly dispersed Au nanoseeds are greatly conducive to the improvement of Li wettability. Moreover, the alloying of Au nanoseeds with deposited Li metal is able to sufficiently eliminate the energy barrier of nucleation, leading to smooth Li plating morphology without Li dendrites. As a result, the Li-Au/Cu nanoscaffold anodes showed ultralow voltage hysteresis and significantly prolonged cycle life in symmetric cells, and also excellent cycle stability and ultrahigh Coulombic efficiency in Li-Au/Cu nanoscaffold‖LFP full batteries. With the Li-Au/Cu nanoscaffold anodes, it is expected to fabricate stable-cycling Li metal-based batteries with outstanding electrochemical performances. This study provides a feasible strategy for the construction of safe and stable Li metal anodes and promoting the practical applications of high-energy-density Li metal batteries.

Supporting Information

Supporting Information is available from the Wiley Online Library or from the author.

Acknowledgements

H.L., Z.Z., and Y.W. contributed equally to this work. This work was supported by the National Key Research and Development Program of China (2017YFA0208200), the National Natural Science Foundation of China (22022505, 21872069, 51761135104), the Fundamental Research Funds for the Central Universities of China (0205-14380219, 0205–14913212), the Natural Science Foundation of Jiangsu Province (BK20180008), and the Shenzhen Fundamental Research Program of Science, Technology and Innovation Commission of Shenzhen Municipality (JCYJ20180307155007589).

Conflict of Interest

The authors declare no conflict of interest.

Data Availability Statement

The data that support the findings of this study are available from the corresponding author upon reasonable request.

Keywords

3D porous nanoscaffold, dendrite growth suppression, heterogeneous nanoseeds, lithium electrodeposition guidance, lithium metal anodes

Received: March 20, 2021
Revised: April 22, 2021
Published online:

[1] P. Simon, Y. Gogotsi, *Nat. Mater.* **2008**, *7*, 845.
[2] B. Dunn, H. Kamath, J. M. Tarascon, *Science* **2011**, *334*, 928.
[3] M. Armand, J. M. Tarascon, *Nature* **2008**, *451*, 652.
[4] J. Xu, J. Ma, Q. Fan, S. Guo, S. Dou, *Adv. Mater.* **2017**, *29*, 1606454.
[5] R. Sarrias-Mena, L. M. Fernández-Ramírez, C. A. García-Vázquez, F. Jurado, *Renewable Sustainable Energy Rev.* **2014**, *34*, 194.
[6] N. L. Panwar, S. C. Kaushik, S. Kothari, *Renewable Sustainable Energy Rev.* **2011**, *15*, 1513.
[7] J. Wandt, C. Marino, H. A. Gasteiger, P. Jakes, R. A. Eichel, J. Granwehr, *Energy Environ. Sci.* **2015**, *8*, 1358.
[8] L. Ji, Z. Lin, M. Alcoutlabi, X. W. Zhang, *Energy Environ. Sci.* **2011**, *4*, 2682.
[9] K. Zhang, G. Lee, M. Park, W. J. Li, Y. Kang, *Adv. Funct. Mater.* **2016**, *6*, 1600811.
[10] K. J. Harry, D. T. Hallinan, D. Y. Parkinson, A. A. MacDowell, N. P. Balsara, *Nat. Mater.* **2014**, *13*, 69.
[11] Y. Lu, Z. Tu, L. A. Archer, *Nat. Mater.* **2014**, *13*, 961.
[12] D. Wang, W. Zhang, W. T. Zheng, X. Q. Cui, T. Rojo, Q. Zhang, *Adv. Sci.* **2017**, *4*, 1600168.
[13] D. Lin, Y. Liu, Y. Cui, *Nat. Nanotechnol.* **2017**, *12*, 194.
[14] J. M. Zheng, M. H. Engelhard, D. H. Mei, S. H. Jiao, B. J. Polzin, J. G. Zhang, W. Xu, *Nat. Energy* **2017**, *2*, 17012.
[15] H. L. Dai, K. Xi, X. Liu, C. Lai, S. Q. Zhang, *J. Am. Chem. Soc.* **2018**, *140*, 17515.
[16] H. L. Dai, X. X. Gu, J. Dong, C. Wang, C. Lai, S. H. Sun, *Nat. Commun.* **2020**, *11*, 643.
[17] D. C. Lin, Y. Y. Liu, W. Chen, G. M. Zhou, K. Liu, B. Dunn, Y. Cui, *Nano Lett.* **2017**, *17*, 3731.
[18] Z. J. Ju, J. W. Nan, Y. Wang, T. F. Liu, J. H. Zheng, H. D. Yuan, O. W. Sheng, C. B. Jin, W. K. Zhang, Z. Jin, H. Tian, Y. J. Liu, X. Y. Tao, *Nat. Commun.* **2020**, *11*, 488.
[19] T. Chen, F. B. Meng, Z. W. Zhang, J. C. Wang, Y. Hu, W. H. Kong, X. L. Zhang, Z. Jin, *Nano Energy* **2020**, *76*, 105068.
[20] X. Y. Yue, X. L. Li, J. Bao, Q. Q. Qiu, T. C. Liu, D. Chen, S. S. Yuan, X. J. Wu, J. Lu, Y. N. Zhou, *Adv. Energy Mater.* **2019**, *9*, 1901491.
[21] H. D. Shi, J. Q. Qin, K. Huang, P. F. Lu, C. F. Zhang, Y. F. Dong, M. Ye, Z. M. Liu, Z. S. Wu, *Angew. Chem., Int. Ed.* **2020**, *59*, 12147.
[22] L. Dong, L. Nie, W. Liu, *Adv. Mater.* **2020**, *32*, 1908494.
[23] F. Zhou, Z. Li, Y. Y. Lu, B. Shen, Y. Guan, X. X. Wang, Y. C. Yin, B. S. Zhu, L. L. Lu, Y. Ni, Y. Cui, H. B. Yao, S. H. Yu, *Nat. Commun.* **2019**, *10*, 2482.
[24] J. Y. Liang, X. X. Zeng, X. D. Zhang, T. T. Zuo, M. Yan, Y. X. Yin, J. L. Shi, X. W. Wu, Y. G. Guo, L. J. Wan, *J. Am. Chem. Soc.* **2019**, *141*, 9165.
[25] Y. T. Li, X. Chen, A. Dolocan, Z. M. Cui, S. Xin, L. G. Xue, H. h. Xu, K. Park, J. B. Goodenough, *J. Am. Chem. Soc.* **2018**, *140*, 6448.
[26] J. Liang, Q. Y. Chen, X. B. Liao, P. C. Yao, B. Zhu, G. X. Lv, X. Y. Wang, X. Chen, J. Zhu, *Angew. Chem., Int. Ed.* **2020**, *59*, 6561.
[27] C. Li, S. Liu, C. Shi, G. Liang, Z. Lu, R. Fu, D. Wu, *Nat. Commun.* **2019**, *10*, 1363.
[28] C. P. Yang, Y. X. Yin, S. F. Zhang, N. Y. Li, Y. G. Guo, *Nat. Commun.* **2015**, *6*, 8058.
[29] Q. B. Yun, Y. B. He, W. Lv, Y. Zhang, B. H. Li, F. Y. Kang, Q. H. Yang, *Adv. Mater.* **2016**, *28*, 6932.
[30] Q. Li, S. P. Zhu, Y. Y. Lu, *Adv. Funct. Mater.* **2017**, *27*, 1606422.
[31] A. Wang, S. Tang, D. Kong, S. Liu, K. Chiou, L. J. Zhi, J. X. Huang, Y. Y. Xiao, J. Y. Luo, *Adv. Mater.* **2017**, *30*, 1703891.
[32] K. Yan, Z. Lu, H. W. Lee, *Nat. Energy* **2016**, *1*, 16010.
[33] C. Yang, Y. Yao, S. He, F. Xiong, P. C. Hu, Y. Z. Li, J. Zhao, S. Chu, Y. Cui, *Adv. Mater.* **2017**, *29*, 1702714.
[34] S. Wu, Z. Zhang, M. Lan, H. Xie, E. Hitz, L. B. Hu, *Adv. Mater.* **2018**, *30*, 1705830.
[35] R. Zhang, X. R. Chen, X. Chen, X. B. Cheng, X. Q. Zhang, C. Yang, Q. Zhang, *Angew. Chem., Int. Ed.* **2017**, *129*, 7764.
[36] S. H. Wang, Y. X. Yin, T. T. Zuo, W. Dong, J. Y. Li, J. L. Shi, C. H. Zheng, N. W. Li, C. J. Li, Y. G. Guo, *Adv. Mater.* **2017**, *29*, 1703729.
[37] L. Liu, Y. X. Yin, J. Y. Li, S. H. Wang, Y. G. Guo, L. J. Wan, *Adv. Mater.* **2018**, *30*, 1706216.
[38] H. Geng, X. Cao, Y. Zhang, K. Geng, G. Qu, M. Tang, *J. Power Sources* **2015**, *294*, 465.
[39] T. L. Kulova, A. M. Skundin, V. M. Kozhevin, D. A. Yavsin, S. A. Gurevich, *Russ. J. Electrochem.* **2010**, *46*, 877.